Physics of Fluids ARTICLE pubs.aip.org/aip/pof

Analysis of the spreading radius in droplet impact: The two-dimensional case

Cite as: Phys. Fluids **35**, 102124 (2023); doi: 10.1063/5.0169274
Submitted: 24 July 2023 · Accepted: 9 October 2023 ·
Published Online: 25 October 2023

Lennon Ó Náraigh[1,a)] and Juan Mairal[2]

AFFILIATIONS

[1]School of Mathematics and Statistics, University College Dublin, Belfield, Dublin 4, Ireland
[2]I3A, University of Zaragoza, Zaragoza, Spain

[a)]Author to whom correspondence should be addressed: onaraigh@maths.ucd.ie

ABSTRACT

We study droplet impact problems in a 3D cylindrical or equivalent 2D Cartesian geometry. Such structures do have an approximate experimental realization, and they are often simulated as a testbed for computational methods. We focus on droplet impact on a smooth homogeneous surface as well as head-on collision of two droplets. We perform an energy-budget analysis and introduce a correlation, which predicts the maximum spreading radius as a function of Reynolds number and Weber number. We show how the dissipation term in this analysis can be decomposed into boundary-layer dissipation in the droplet lamella (where applicable) and head loss. We use existing results in the literature (simulations and experiments) as well as our own simulation results to validate the correlation. Dissipation by head loss is a key term in the analysis: only by modeling it accurately, one can obtain good agreement between the simulations and the theory.

I. INTRODUCTION

The impact of a droplet of fluid on a smooth, homogeneous substrate is a well studied problem, with many practical applications, e.g., inkjet printing,[1] cooling,[1,2] and crop spraying.[1,3] The phenomenon has been studied using experimental,[4–6] theoretical,[7,8] and computational[9–11] techniques. Different impact regimes occur depending on the droplet's Weber number and Reynolds number. The literature pertaining to the mapping of the different regimes is vast, and the problem is not yet fully understood. The reader is referred to the extensive review papers by Yarin *et al.*[1] and Josserand and Thoroddsen[12] for an overview. It is well known that there is a splashing threshold $\mathrm{We}\sqrt{\mathrm{Re}} \lesssim 3000$, below which the impacting droplet retains an axisymmetric shape and spreads across the substrate until a maximum spreading radius is attained, whereupon retraction occurs.[12] Naturally, this is a 3D (albeit axisymmetric) phenomenon. However, in a recent experiment by Lejeune *et al.*,[13] rectangular liquid sheets have been created after an asymmetric droplet impact. In a more recent experiment by Néel *et al.*,[14] the authors created toroidal liquid cylinders, which were then subjected to a head-on collision. In this second experiment, the resulting spreading phenomenon is qualitatively different to what would be observed in a 3D axisymmetric head-on collision. The authors introduce a theoretical description of the droplet impact based on an idealized cylindrical droplet. Further theoretical analysis of droplet impact and droplet spread in the case of liquid cylinders may be useful to understand these experiments.

A second motivation is that many computational studies have been performed in the case of droplet impact and droplet spread for such (idealized) 2D systems.[15–20] These simulations have been performed as testbeds either for the analogous but more complex 3D axisymmetric geometry or for fully 3D non-axisymmetric geometry. As a part of these test simulations, the authors analyze the extent to which the droplet spreads after impact, as a function of time. Maximum spreading occurs just before retraction. The maximum spreading radius is a function of Weber number and Reynolds number. Analogous to the 3D case, Gupta and Kumar[17] developed a theoretical correlation for the maximum spreading radius as a function of Reynolds number, Weber number, and contact angle. The correlation is based on an energy-budget analysis. The authors compare their theoretical analysis with computational results, and excellent agreement is obtained. The computational results are restricted to low density ratios (<10) and to high Weber number (>180). The present study looks at a density ratio of 1000, typical of an air–water system. The focus herein is on lower Weber numbers. As such, the present study is complementary to that of Gupta and Kumar.

Energy-budget analysis is an important tool for estimating the maximum droplet spread in the 3D case.[4,21] The analysis involves

relating the pre-impact energy of the droplet to the post-impact energy at maximum spreading, of which the latter can be assumed to be entirely due to surface energy. Viscous dissipation is incorporated into the energy budget by explicitly modeling the boundary layer in the lamella. By treating the droplet at maximum spreading as having a pancake-like structure, a simple closed expression can be found for the maximum spreading ratio as a function of Weber number and Reynolds number.

In the 3D case, the energy-budget analysis for the maximum spreading radius is known to over-predict the maximum spreading radius in the rim-lamella regime.[22] This refers to a regime at a large Weber number and an intermediate Reynolds number where in the extremity of the spreading droplet forms a "bulge" or rim, the dynamics of which are governed by surface tension. In this case, a rim-lamella model[11] (often coupled with an energy-budget analysis[7]) is used to predict the maximum spreading radius. Motivated by these observations, the main aim of the present work is to develop an energy-budget analysis in the case of 2D droplets (or equivalently, 3D cylindrical droplets) and to correct for the rim. In this way, we will develop predictions for the maximum spreading radius and compare these to simulation data and experiments.

A. Terminology and notation

Throughout this work, we refer to 3D cylindrical droplets and 2D droplets interchangeably, as these are mathematically equivalent. Hence, we are dealing with a cylinder of liquid that impacts a surface along the cylinder's axis. Certainly, such a scenario is an idealization, although it is an important computational test case, as alluded to previously. Furthermore, in the experiments by Néel *et al.*,[14] the quasi-2D toroidal liquid cylinders remain quasi-2D after the collision below a critical Reynolds number and Weber number. This is analogous to the splash threshold in 3D spherical droplet splash and droplet impact problems. In this case, if the major radius of the torus is large compared to the minor one, the droplet impact problem can be modeled as one involving idealized 3D cylindrical droplets.

Throughout the work, we use the following definitions for the Weber number and Reynolds number:

$$\mathrm{We} = \frac{\rho U_0^2 R_0}{\sigma}, \quad \mathrm{Re} = \frac{\rho U_0 R_0}{\mu}, \tag{1}$$

where ρ is the drop-side fluid density, σ is the surface tension, and μ is the drop-side fluid viscosity. Also, U_0 is the droplet's speed prior to impact, and R_0 is the radius of the droplet prior to impact. We use the notation $r_{\max}$ to denote the maximum spreading radius of the droplet after impact, and the variable $\beta_{\max} = r_{\max}/R_0$ to denote the non-dimensional maximum spreading radius.

B. Layout of the paper

This paper is organized as follows: In Sec. II, we introduce a theoretical model for the maximum spreading radius in 2D droplet impact problems. As we are interested in comparing the theoretical model with evidence from simulations, we present a method for generating such simulations in Sec. III, based on the diffuse interface method. We compare the theoretical model with our own simulation results in the case of droplet impact on a smooth surface in Sec. IV. We compare the predictions of the theoretical model with simulation results (both our own and other results drawn from the literature) in the case of head-on droplet collision in Sec. V. We also compare the predictions of the theoretical model with simulation results. The conclusions are presented in Sec. VI.

II. THEORETICAL MODEL

In general, there is no analytical formula for $r_{\max}(\mathrm{We}, \mathrm{Re})$. In the case of 3D axisymmetric droplets, a number of correlations exist in the literature. At least three approaches to formulating the correlation exist. The first involves semi-empirical formulas based on a very wide range of experimental results, such as the work by Roisman,[23] where the 3D leading-order scaling $r_{\max} \sim \mathrm{Re}^{1/5}$ is elucidated, in the case of the viscous-spreading regime ($P > 1$, $P = \mathrm{We}/\mathrm{Re}^{4/5}$). A second approach involves an energy-budget analysis, wherein the pre-impact energy of the droplet is equated to the energy at maximum spreading, plus the energy dissipated.[4,22] A third approach, based on momentum balances, is valid in the rim-lamella regime of droplet spreading.[7,11] All approaches generate equivalent scaling behaviors in the appropriate asymptotic limits. For the present purposes, we use the energy-budget analysis, tailored to 2D droplets, and pay particular attention to the modeling of the energy dissipation, which is key to producing a correlation that matches the available experimental and simulation data.

A. Energy-budget analysis

For a cylindrical drop with pre-impact speed U_0 and radius R_0, the initial energy of the system is

$$E_{\mathrm{init}} = \left[\frac{1}{2}\rho(\pi R_0^2)U_0^2 + 2\pi R_0 \sigma\right]\lambda, \tag{2}$$

where λ is the length of the cylindrical droplet in the third dimension; this is an irrelevant variable as it cancels from both sides of the following energy-budget analysis. At maximum spreading, it is assumed that the droplet's internal kinetic energy is negligible, such that the droplet's energy can be attributed entirely to surface energy,

$$E_{\mathrm{final}} = \sigma(\Pi - 2r_{\max}\cos\vartheta)\lambda. \tag{3}$$

Here, Π is the perimeter of the droplet at maximum spread, and ϑ is the advancing contact angle. Equations (2) and (3) are explained in more detail in Appendix. The initial and final energies are related through an energy balance,

$$E_{\mathrm{init}} = E_{\mathrm{final}} + \Delta E, \tag{4}$$

where ΔE denotes the energy loss through viscous dissipation.

According to Wildeman *et al.*,[22] the energy loss due to viscous dissipation is made up of at least two parts, corresponding to losses in the rim and the lamella. These regions are shown schematically in Fig. 1. The first part is viscous dissipation due to a boundary layer, which forms inside the droplet lamella. The thickness of the boundary layer is estimated as $\delta \sim \sqrt{\nu\tau}$, where ν is the liquid kinematic viscosity, and τ is the time interval between the formation of the boundary layer and the time of maximum droplet spread. Hence, $\Delta E_{bl} \sim \mu(U_0/\delta)^2[\delta(2r_{\max})\lambda]\tau$. We estimate $\tau \approx (r_{\max}/U_0) - (R_0/U_0)$, that is, the time for maximum spread to occur, minus a time interval R_0/U_0 of an initial phase prior to the onset of the boundary layer. Hence, the energy loss due to the boundary layer is estimated as follows:

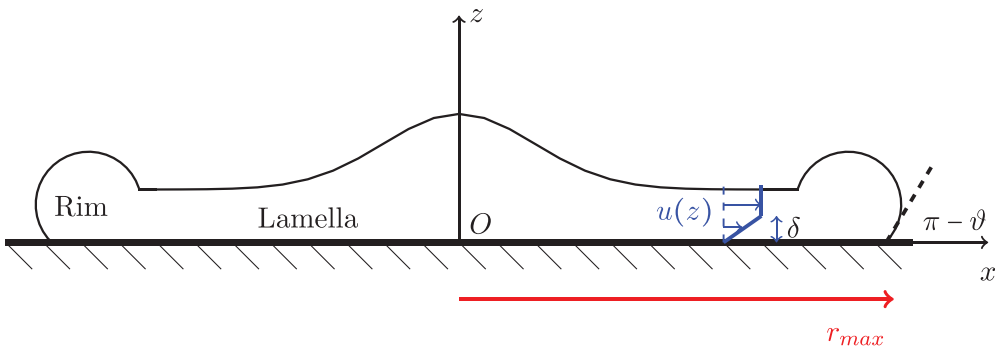

FIG. 1. Schematic diagram showing the rim-lamella structure of the droplet at maximum spreading. The figure also shows the flow profile $u(z)$ including the boundary layer of thickness δ.

$$\Delta E_{bl} \approx \frac{2a}{\sqrt{\mathrm{Re}}}\rho U_0^2 \beta_{\max}\sqrt{\beta_{\max}-1}(R_0^2\lambda), \tag{5}$$

where a is an $O(1)$ constant, and $\beta_{\max} = r_{\max}/R_0$.

A second source of dissipation is the so-called head loss. Classically, "head loss" (e.g., in a pipe flow) refers to the loss of pressure head due to wall friction (major head loss) or to loss of pressure due to sharp changes in the pipe geometry, which lead to recirculation zones (minor head loss). Minor head loss is analogous to the scenario that occurs when the flow in the lamella passes into the rim. According to Wildemen *et al.*[22] and Villermaux and Bossa,[24] the head loss can be estimated as a simple fraction of the initial kinetic energy of the droplet prior to impact. As viscous dissipation prior to impact is negligible, the kinetic energy of the droplet prior to impact corresponds almost exactly to the initial potential energy of the droplet, $(1/2)\rho(\pi R_0^2)U_0^2\lambda$. Thus, the head loss is estimated as follows:

$$\Delta E_h \approx b\left[\frac{1}{2}\rho(\pi R_0^2)U_0^2\lambda\right], \tag{6}$$

where $0 < b < 1$ is another constant. In this way, the energy budget (4) becomes

$$\frac{1}{2}\rho(\pi R_0^2)U_0^2 + 2\pi R_0\sigma = \sigma(\Pi - 2r_{\max}\cos\vartheta) + \frac{2a}{\sqrt{\mathrm{Re}}}\rho U_0^2\beta_{\max}\sqrt{\beta_{\max}-1}\,R_0^2 + b\left[\frac{1}{2}\rho(\pi R_0^2)U_0^2\right]. \tag{7}$$

A third loss channel active at a low Weber number has been identified by Park *et al.*[25] and Huang and Chen.[26] This is the phenomenon of spontaneous surface dissipation. This is absent from previous studies at a high Weber number (e.g., by Wildeman *et al.*[22] and Roisman *et al.*[7]), but is relevant in the present study. However, this loss channel can be incorporated into the expression for head loss: as such, Eq. (6) represents energy losses through all channels other than boundary-layer dissipation.

We now divide Eq. (7) across by $(1/2)\rho(\pi R_0^2)U_0^2$ to obtain

$$(1-b) + \frac{4}{\mathrm{We}} = \frac{2}{\pi\mathrm{We}}\left(\frac{\Pi}{R_0} - 2\beta_{\max}\cos\vartheta\right) + \frac{4}{\pi}\frac{a}{\sqrt{\mathrm{Re}}}\beta_{\max}\sqrt{\beta_{\max}-1}. \tag{8}$$

To make further progress, it is necessary to have an expression for the droplet perimeter Π. A rough approximation can be made by treating the droplet as a rectangle. The equivalent 3D approximation would be a disk, and this is a standard approach in the literature.[4] The droplet area is fixed as $A_0 = \pi R_0^2$, and this is then equal to the droplet area at maximum spread, $A_0 = 2r_{\max}h$, where h is the height of the droplet at maximum spread. Hence, the perimeter is approximated as $\Pi = 2r_{\max} + A_0/r_{\max}$. Thus, Eq. (8) becomes

$$(1-b) + \frac{4}{\mathrm{We}} = \frac{2}{\pi\mathrm{We}}\left[2\beta_{\max}(1-\cos\vartheta) + \frac{\pi}{\beta_{\max}}\right] + \frac{a}{\sqrt{\mathrm{Re}}}\beta_{\max}\sqrt{\beta_{\max}-1}. \tag{9}$$

(the factor of $4/\pi$ in the dissipation term has been absorbed into a). Equation (9) does not have an explicit solution for $\beta_{\max}$ in terms of We and Re; however, it can be solved numerically for the purpose of comparing with experiments and simulations. Furthermore, explicit solutions exist in certain limiting cases.

B. Asymptotic limits

We now examine some special limiting cases of Eq. (9) where an explicit expression for $\beta_{\max}$ is possible.

1. Inviscid limit

For $\mathrm{Re} \to \infty$, Eq. (9) reduces to

$$\frac{\pi}{2}(1-b)\mathrm{We} + 2\pi = \left[2\beta_{\max}(1-\cos\vartheta) + \frac{\pi}{\beta_{\max}}\right], \tag{10}$$

with exact solution

$$\beta_{\max} = \frac{\omega + \sqrt{\omega^2 - 8\pi(1-\cos\vartheta)}}{4(1-\cos\vartheta)}, \quad \omega = \frac{\pi}{2}(1-b)\mathrm{We} + 2\pi. \tag{11}$$

For We large but finite, this further reduces to

$$\beta_{\max} \approx \frac{\mathrm{We}\,\pi(1-b)}{4(1-\cos\vartheta)}. \tag{12}$$

The equivalent scaling behavior for 3D axisymmetric droplets is

$$\beta_{\max} \approx \sqrt{\frac{4}{1-\cos\vartheta}\left[\frac{1}{12}(1-b)\mathrm{We}+1\right]}. \tag{13}$$

Hence, $\beta_{\max} \sim \mathrm{We}$ for cylindrical droplets, and $\beta_{\max} \sim \mathrm{We}^{1/2}$ for axisymmetric droplets.

2. Finite viscosity, large Weber number

For $\mathrm{We} \to \infty$, Eq. (9) reduces to

$$\frac{\pi}{2}(1-b) \approx \frac{2a}{\sqrt{\mathrm{Re}}}\beta_{\max}\sqrt{\beta_{\max}-1}. \tag{14}$$

For Re large but finite, this gives $\beta_{\max} \sim \mathrm{Re}^{1/3}$. The corresponding result for 3D axisymmetric droplets is $\beta_{\max} \sim \mathrm{Re}^{1/5}$.

C. Head-on collision of two droplets

The head-on collision of two 2D droplets has been investigated by Wu *et al.*[19] In a previous study,[27] in the case of 3D axisymmetric droplets, it is argued that the head-on collision of two such droplets is equivalent (in terms of energy-budget analysis) to a droplet impacting on a surface with a free-slip boundary condition and a contact angle of $\pi/2$. Studies of collisions of head-on droplets also have applications in understanding atmospheric raindrop formation and droplet collision in combustion and agricultural sprays.[27]

In this scenario, there is no viscous boundary layer. As such, an appropriate correlation for the head-on collision of two droplets in 2D is simply Eq. (10), with $\vartheta = \pi/2$,

$$\frac{\pi}{2}(1-b)\mathrm{We} + 2\pi = \left(2\beta_{\max} + \frac{\pi}{\beta_{\max}}\right). \tag{15}$$

In the limit of large We, this again gives $\beta_{\max} \sim \mathrm{We}$, i.e., linear scaling. This scaling behavior has been observed in experiments, which we document in Sec. V.

III. NUMERICAL METHOD

The aim of the present work is to validate the correlations developed in Sec. II, using data from simulations and experiments. We use simulation data from the literature, supplemented with our own. For the latter purpose, we use a diffuse interface method to model droplet impact and droplet collisions. We summarize the methodology below.

A. Diffuse-interface method

We use the diffuse-interface method to describe the interface separating the gas from the liquid. A phase-field function $C(\boldsymbol{x}, t)$ is introduced, with (conventionally) $C=1$ indicating the liquid phase and $C=-1$ the surrounding gas phase. Thus, $C(\boldsymbol{x}, t) = 1$ if the region around the point $\boldsymbol{x}$ is rich in liquid phase at time t, and $C(\boldsymbol{x}, t) = -1$ if the region around the same point is rich in the gas phase. Also, the level set $C=0$ represents a demarcation between the liquid and the gas phases. In this approach, the energy associated with interfaces is estimated from a diffuse-interface functional,

$$F[C] = \frac{\hat{\sigma}}{\xi}\int_\Omega \left[f_0(C) + \frac{1}{2}\xi^2|\nabla C|^2\right]\mathrm{d}^3x. \tag{16}$$

Here, $\hat{\sigma}$ is a constant with units of surface tension, and Ω is the fluid domain. The evolution for C is given by

$$\frac{\partial C}{\partial t} + \boldsymbol{u}\cdot\nabla C = \nabla\cdot[M(C)\nabla\Phi], \tag{17a}$$

where $M(C) \geq 0$ is a non-negative mobility function, and

$$\Phi = \delta F/\delta C = \frac{\hat{\sigma}}{\xi}\left[f_0'(C) - \xi^2\nabla^2 C\right]. \tag{17b}$$

The diffuse-interface method is essentially a "one-fluid" formulation. As such, there is a single fluid velocity $\boldsymbol{u}(\boldsymbol{x}, t)$, a single fluid density, and a single fluid viscosity. However, the fluid density ρ and fluid viscosity μ depend on the amount of each fluid phase present at a particular point,

$$\rho = \rho_G\left[\frac{1}{2}(1-C)\right] + \rho_L\left[\frac{1}{2}(1+C)\right], \tag{18a}$$

$$\mu = \mu_G\left[\frac{1}{2}(1-C)\right] + \mu_L\left[\frac{1}{2}(1+C)\right]. \tag{18b}$$

Here, ρ_L and ρ_G are the constant densities in each of the pure fluid phases (liquid and gas in the present context), and μ_L and μ_G are the constant dynamic viscosities in the same. We emphasize that in contrast to the other sections, in this section and this section only we use ρ for the variable density in the one-fluid formulation and ρ_L and ρ_G for the (constant) liquid and gas densities, whereas in the other sections, we use ρ for the constant liquid density. A similar statement applies to μ, μ_L, and μ_G.

The velocity field $\boldsymbol{u}(\boldsymbol{x}, t)$ then satisfies a Navier–Stokes equation with a Korteweg stress term,

$$\rho\left(\frac{\partial \boldsymbol{u}}{\partial t} + \boldsymbol{u}\cdot\nabla\boldsymbol{u}\right) = -\nabla p + \nabla\cdot\left[\mu(\nabla\boldsymbol{u} + \nabla\boldsymbol{u}^T)\right] + \Phi\nabla C + \rho\boldsymbol{g}. \tag{19}$$

The Korteweg stress term is $\Phi\nabla C$, and this describes the effect of surface tension in the diffuse-interface formalism. Here also, $\boldsymbol{g}$ is the acceleration due to gravity.

Finally, we comment on the choice of interpolation in Eq. (18), as this is influenced by the mobility function $M(C)$. This is often taken to be C-dependent; this guarantees $|C| \leq 1$. Following Ewetola *et al.*,[28] and for simplicity, we take the mobility $M(C)$ to be a constant. This choice occasionally produces values of C such that $|C| > 1$. When this occurs, the expressions (18) are modified, e.g., the expression for the density becomes

$$\rho = \rho_G\min\left\{-1, \left[\frac{1}{2}(1-C)\right]\right\} + \rho_L\max\left\{1, \left[\frac{1}{2}(1+C)\right]\right\}, \tag{20}$$

and a similar expression then applies to the viscosity.

In summary, the diffuse-interface model consists of four equations: Eq. (17) for the phase field C, Eq. (18) for interpolating the density and viscosity between the different fluid phases, Eq. (19) for the velocity field $\boldsymbol{u}$, and finally, a mass-conservation equation, which we take to be the incompressibility condition,

$$\nabla\cdot\boldsymbol{u} = 0. \tag{21}$$

The equations of motion for the diffuse interface method are implemented using an established in-house computational framework based on prior works.[29–31]

Mass conservation $(d/dt)\int_\Omega C\mathrm{d}^3x = 0$ is further ensured by taking $\hat{\boldsymbol{n}}_f \cdot \nabla\Phi = 0$ on $\partial\Omega$, the boundary of the domain Ω, and here, $\hat{\boldsymbol{n}}_f$ is the outward-pointing unit normal to $\partial\Omega$. Also, the no-slip condition $\boldsymbol{u} = 0$ is applied on $\partial\Omega$. However, because Eq. (17) is a fourth-order partial-differential equation, a further boundary condition is needed. The freedom afforded by the extra boundary condition enables us to prescribe the behavior of the contact line. On boundary faces where a contact line exists, we impose the so-called geometric boundary condition,[32]

$$\hat{\boldsymbol{n}}_f \cdot \nabla C = -\tan\left(\frac{1}{2}\pi - \vartheta\right)|\nabla C - (\hat{\boldsymbol{n}}_f \cdot \nabla C)\hat{\boldsymbol{n}}_f|, \tag{22}$$

where ϑ_0 is the static contact angle. Using this geometric condition gives the same results as other boundary conditions based on free-energy arguments.[28,32]

B. Choice of diffuse-interface parameters

We use the diffuse-interface method to model droplet impact and droplet spread on a smooth surface. In dimensionless variables, the Cahn–Hilliard Eq. (17) describing the interface location becomes

$$\frac{\partial C}{\partial t} + \boldsymbol{u}\cdot\nabla C = \mathcal{D}\nabla^2\left[f_0'(C) - \mathrm{Cn}^2\nabla^2 C\right], \qquad \mathcal{D} = \frac{R_0}{\xi}\frac{M_0\hat{\sigma}}{UL^2}, \quad \mathrm{Cn} = \xi/R_0, \tag{23}$$

where $M_0 \geq 0$ is the constant mobility. We identify the Cahn number $\mathrm{Cn} = \xi/R_0$ and the interfacial Péclet number $\mathrm{Pe} = UL^2/(M_0\hat{\sigma})$. The coefficient $\hat{\sigma}$ is related to the surface tension. This statement can be made precise through the following equation:

$$\sigma = \xi\hat{\sigma}\int_{-\infty}^{\infty}\left(\frac{\mathrm{d}C_*}{\mathrm{d}z}\right)^2\mathrm{d}z, \tag{24}$$

where we have reverted momentarily to the dimensional variables. Here, $C_* = \tanh\left(z/\sqrt{2}\xi\right)$ is the equilibrium one-interface solution to the Cahn–Hilliard equation in the absence of flow. The justification for Eq. (24) was given by Ding *et al.*[15] Using Eq. (24), we obtain $\hat{\sigma} = \left(3/2\sqrt{2}\right)\sigma$. Thus, the dimensionless Navier–Stokes equations with surface tension now read

$$\hat{\rho}\left(\frac{\partial \boldsymbol{u}}{\partial t} + \boldsymbol{u}\cdot\nabla\boldsymbol{u}\right) = -\nabla p + \frac{1}{\mathrm{Re}}\nabla\cdot\left[\hat{\mu}(\nabla\boldsymbol{u} + \nabla\boldsymbol{u}^T)\right] + \frac{3}{2\sqrt{2}}\frac{1}{\mathrm{Cn}}\frac{1}{\mathrm{Bo}}\left[f_0'(C) - \mathrm{Cn}^2\nabla^2 C\right]\nabla C - \hat{\rho}\,\hat{\boldsymbol{e}}_3, \tag{25a}$$

where

$$\hat{\rho} = \frac{\rho_G}{\rho_L}\min\left\{-1, \left[\frac{1}{2}(1-C)\right]\right\} + \max\left\{1, \left[\frac{1}{2}(1+C)\right]\right\} \tag{25b}$$

and

$$\hat{\mu} = \frac{\mu_G}{\mu_L}\min\left\{-1, \left[\frac{1}{2}(1-C)\right]\right\} + \max\left\{1, \left[\frac{1}{2}(1+C)\right]\right\}, \tag{25c}$$

where $\hat{\boldsymbol{e}}_3$ is the unit vector in the z-direction. The incompressibility condition $\nabla\cdot\boldsymbol{u} = 0$ is unchanged.

IV. COMPARISON WITH SIMULATIONS: DROPLET IMPACT ON A SURFACE

In this section, we generate data using numerical simulations of a 2D droplet impacting on a solid surface, at various values of the equilibrium contact angle. In this way, we aim to build up a database of simulation results to validate the correlations introduced in Sec. II. We first of all describe the setup of a test case, we then carefully analyze the convergence of the numerical results, and finally, we compare the simulation data to the correlations. Throughout, we use the diffuse interface method introduced in Sec. III.

A. Test case

To fix ideas, we focus on a particular case study, corresponding to a millimeter-scale water droplet falling in air, and this is relevant to the industrial applications mentioned in the introduction. The parameters of the test case are given in Table I. We present our results in non-dimensional variables. Length scales are made non-dimensional on the droplet radius R_0, and time is made dimensionless using the Bond timescale $T = R_0/U_0$, where $U_0 = \sqrt{gR_0}$, and $g = 9.81\,\mathrm{ms}^{-2}$ is the acceleration due to gravity. Densities and viscosities are made dimensionless on the liquid values. Thus, in dimensionless variables, the acceleration due to gravity has unit strength. The use of $\sqrt{gR_0}$ as the characteristic velocity in this section means that the strength of the surface tension is $1/\mathrm{Bo}$, where

$$\mathrm{Bo} = \frac{\rho_L g R_0^2}{\sigma} \tag{26}$$

is the Bond number. Note that with $U_0 = \sqrt{gR_0}$, Eq. (26) also describes a Weber number $\rho_L U_0^2 R_0/\sigma$.

In the same way, the strength of the viscosity in dimensionless terms is $1/\mathrm{Re}$, where

$$\mathrm{Re} = \frac{\rho_L R_0 U_0}{\mu_L} = \frac{\rho_L g^{1/2} R_0^{3/2}}{\mu_L}. \tag{27}$$

With the values in Table I, we have $\mathrm{Bo} = 1.226$ and $\mathrm{Re} = 578.0$. Unless otherwise stated, in the rest of the work, results and discussion are presented in dimensionless variables.

We carry out simulations in a 2D Cartesian geometry with the following domain:

$$\Omega = \left\{(x,y)|\, -\frac{1}{2}L_x < x < \frac{1}{2}L_x, 0 < z < L_z\right\}, \tag{28}$$

where the value $L_z = 6R_0$ is chosen. Similarly, L_x is chosen to be a multiple of R_0, with the exact value depending on the context. Gravity

TABLE I. Physical parameters used for the test-case simulations. A subscript *L* is used to label water-based quantities, and a subscript *G* is used to label air-based quantities.

	Water (L)	Air (G)
Dynamic viscosity (μ)	8.9×10^{-4} Pas	1.837×10^{-5} Pas
Density (ρ)	$1000\,\mathrm{kgm}^{-3}$	$1.225\,\mathrm{kgm}^{-3}$
Droplet radius (R_0)	3 mm	
Surface tension (σ)	$0.072\,\mathrm{Nm}^{-1}$	

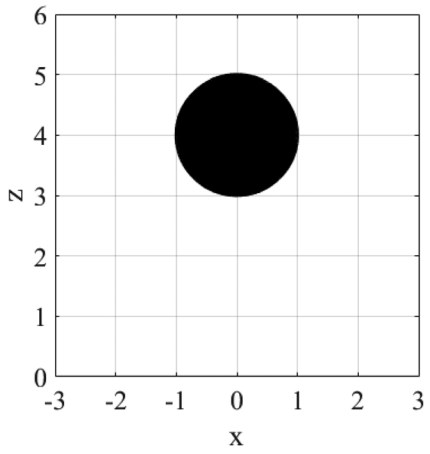

FIG. 2. Initial condition of the droplet.

points in the negative z-direction. Periodic boundary conditions on $\boldsymbol{u}$ are employed in the x-direction and no-slip boundary conditions on the walls at $z=0$ and L_z. The simulations are initialized with zero velocity and zero pressure, and the droplet is released from rest with its center initial located at $z = 4R_0$ (e.g., Fig. 2). The pressure inside the droplet rapidly adjusts to take account of the Laplace pressure jump across the droplet interface.

B. Benchmark result and convergence study

We first of all look at a case where the static contact angle $\vartheta_0 = 90°$, in this way, the boundary condition (22) becomes $\hat{\boldsymbol{n}}_f \cdot \nabla C = 0$ at $z=0$. Figure 2 shows the initial droplet state. Thereafter, the droplet falls and impacts the substrate at dimensionless time $t \approx 2.5$ (0.045 s). After the impact, the spreading phase takes place until maximum spreading is reached at dimensionless time $t \approx 6.0$. Figures 3 and 4 show this process in a diffuse interface simulation with static contact angle $\vartheta_0 = 90°$ and a mesh with 321 cells in the z-direction. After the droplet has reached its maximum extent, the receding phase starts and the droplet contracts, as seen in Fig. 4. At the end of the receding phase, the droplet adopts a compact shape [e.g., Fig. 4(d)], reminiscent of the moments just after the initial impact.

The instantaneous streamfunction at $t=6.1$ is shown in Fig. 5, near the point of maximum spreading. Near $x=0$, the flow resembles that near a stagnation point, this corresponds to a region where the droplet resembles a thin sheet (the "lamella"). However, far from $x=0$, in the bulbous liquid region close to the droplet edge (the "rim"), there is a recirculation zone. These flows generate substantial amounts of dissipation. In Fig. 6, we plot the dissipation function $\text{Diss} = (\hat{\mu}/\text{Re})(u_x^2 + u_z^2 + w_x^2 + w_z^2)$, again at $t=6.1$. There is a large contribution to the dissipation due to the boundary layer in the droplet lamella. A second large contribution inside the droplet rim is also an evidence in the figure, this can be associated with a boundary layer, which forms inside the rim itself, and this arises due to the flow, which circulates inside the droplet rim. There is a third seemingly large contribution to the dissipation at the contact line itself. However, this contribution occurs over a very small region (around 20 grid points in each direction). The total dissipation $\int_\Omega (\text{Diss}) \mathrm{d}^2x$ is measured to be 0.191, and the total dissipation without this small region included is measured to be 0.189, a 1% difference. Thus, this third contribution to the total dissipation is not very important.

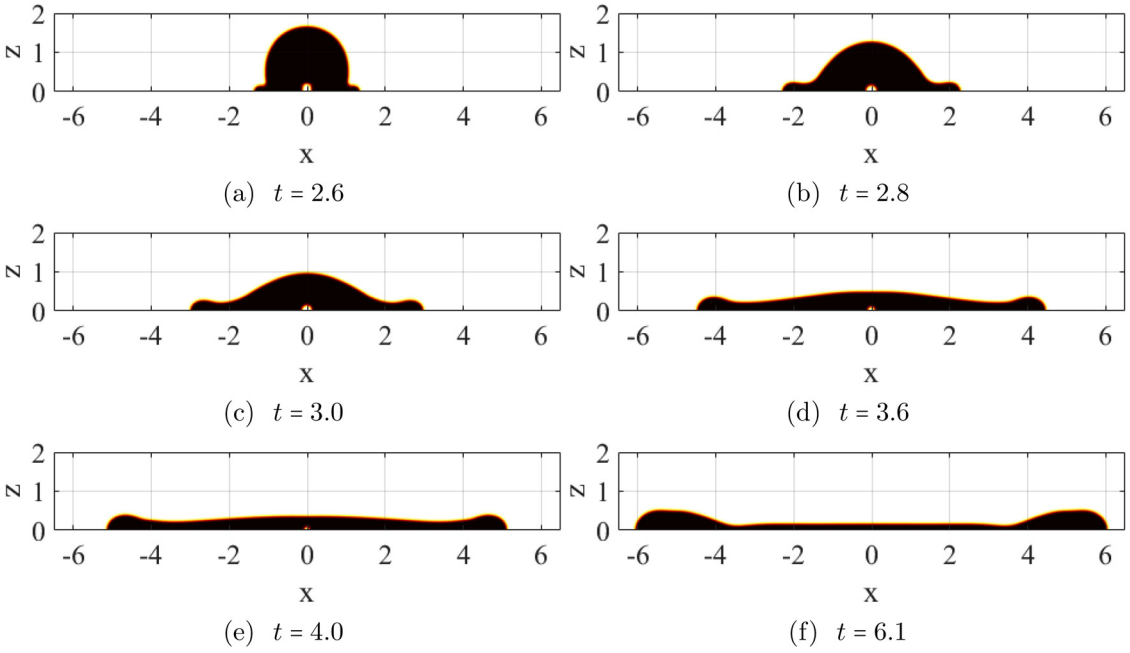

FIG. 3. Sequence of states during the droplet spreading phase. (a) $t=2.6$, (b) $t=2.8$, (c) $t=3.0$, (d) $t=3.6$, (e) $t=4.0$, and (f) $t=6.1$. Parameter values: $\vartheta_0 = 90°$, Bo = 1.226, and Re = 578.0.

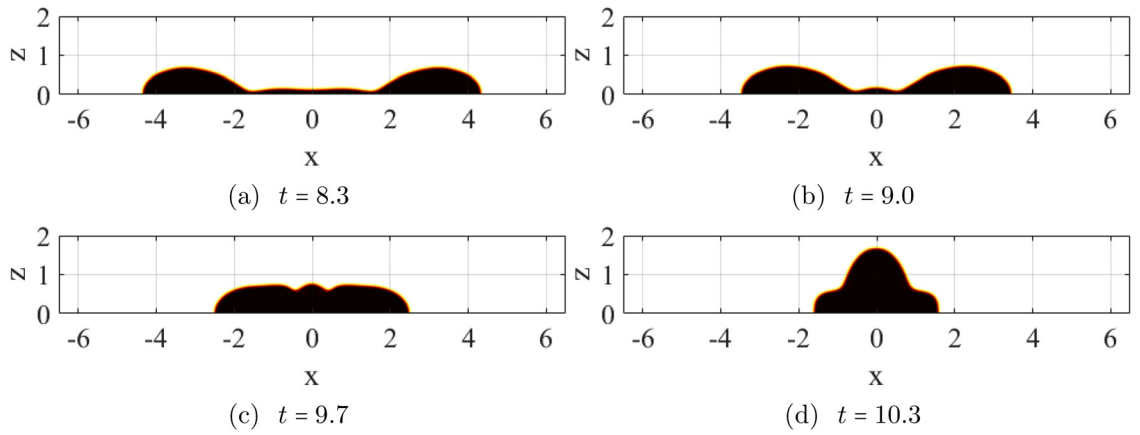

FIG. 4. Sequence of states during the droplet receding phase. (a) $t = 8.3$, (b) $t = 9.0$, (c) $t = 9.7$, and (d) $t = 10.3$. Parameter values: $\vartheta_0 = 90^\circ$, Bo = 1.226, and Re = 578.0.

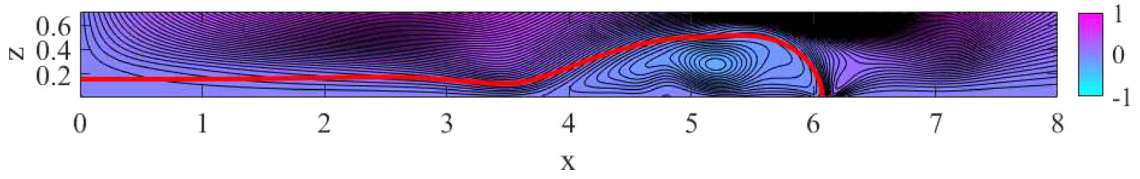

FIG. 5. Instantaneous streamfunction at $t = 6.1$, corresponding to Fig. 3(f), near the point of maximum droplet spreading. To present both axes on the same scale clearly, only the positive half-space $x > 0$ is shown.

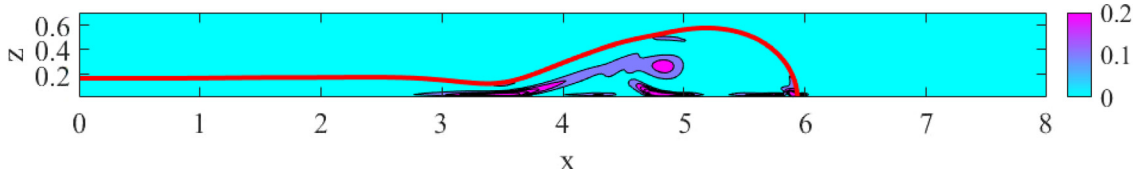

FIG. 6. Instantaneous dissipation function Diss $= (\hat{\mu}/\mathrm{Re})(u_x^2 + u_z^2 + w_x^2 + w_z^2)$ at $t = 6.1$, corresponding to Fig. 3(f), near the point of maximum droplet spreading. To present both axes on the same scale clearly, only the positive half-space $x > 0$ is shown.

We also show the convergence of the numerical simulations with respect to grid refinement. Hence, different uniform meshes are prepared (with $\Delta x = \Delta z$), each characterized by the number of cells in the vertical direction (denoted by N). Following standard practice,[33] the Cahn number varies as $\mathrm{Cn} \propto \Delta x$. The parameters used in the convergence study are shown in Table II. The results are shown in Fig. 7,

TABLE II. Convergence study for the diffuse interface method, for $\vartheta_0 = 90^\circ$. To ensure a CFL number less than one, the time step is halved for the $N = 641$ case.

N	Δt	Δx	Cn	$\mathcal{D}$	Label
161	10^{-4}	0.0375	$(4/3)\Delta x$	Δx	Coarse
321	10^{-4}	0.018 75	⋯	⋯	Standard
641	$10^{-4}/2$	0.009 375	⋯	⋯	Fine

where the spreading ratio $\beta(t)$ of the droplet is plotted against time. This ratio is calculated as $\beta(t) = r(t)/R_0$, where $r(t)$ is the maximum extent of the droplet as it spreads across the substrate, at time t, and R_0 is the initial radius of the droplet. Clearly, convergence of the numerical method is achieved on all meshes used. For the remainder of the work, the "standard" mesh with 321 grid points in the z-direction is used.

From Fig. 7, it is also seen that the initial phase of the droplet spreading is characterized by the relation $\beta(t) \propto (t - t_{\mathrm{impact}})^{1/2}$, where t_{impact} is the time of the initial droplet impact. This scaling is shown in the inset of Fig. 7 and is consistent with a balance between the capillary pressure and the inertial pressure at the contact line,[34] valid just after droplet impact. Specifically, the balance is $\rho_L(\mathrm{d}r/\mathrm{d}t)^2 \propto \sigma R_0/r^2$. Finally, a key conclusion from Fig. 7 is that the simulations are independent of mesh size for the parameters chosen in Table II. Therefore, throughout the remainder of the work, the standard mesh resolution is used.

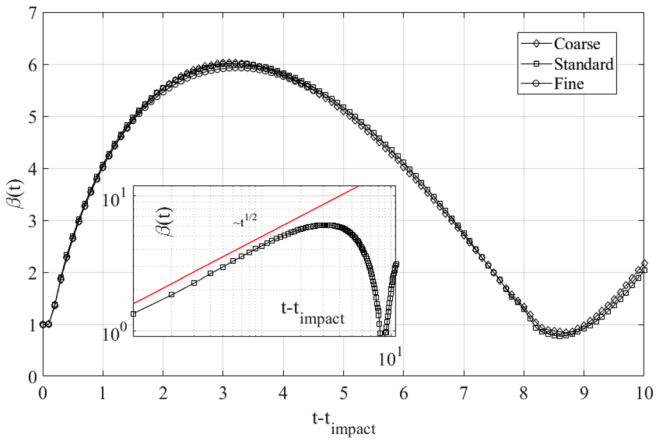

FIG. 7. Spreading ratio of the droplet showing the attainment of grid-independent results. Inset—the same as the main figure, only using a log–log scale, and with $t - t_{\text{impact}}$ on the horizontal axis. Here, t_{impact} refers to the time of droplet impact. Parameters: $\vartheta_0 = 90^\circ$, Bo = 1.226, and Re = 578.0.

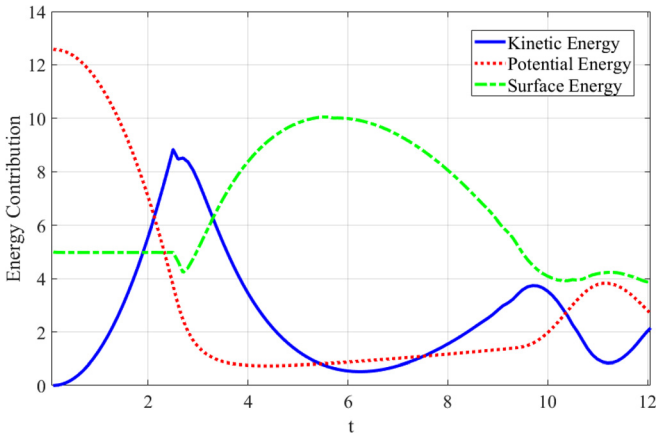

FIG. 8. Energy budget for the case $\vartheta_0 = 90^\circ$. Other parameters: Bo = 1.226 and Re = 578.0.

To further understand the droplet-spreading dynamics up to the point of maximum spread, we look at the total energy of the droplet, made up of kinetic energy, potential energy, and dimensionless surface energy,

$$E_D = \int_\Omega \left(\frac{1}{2}\boldsymbol{u}^2 + z\right)\left[\frac{1}{2}(1+C)\right] \mathrm{d}^3x + F[C]. \tag{29}$$

Here, the non-dimensionalization is with respect to the velocity scale $U_0 = \sqrt{gR_0}$ and the length scale R_0, the same as Eqs. (26) and (27). As we are working in a 2D/3D cylindrical droplet configuration, the relevant dimensions are x and z, the third dimension into the plane of the page can be ignored. The total system energy involves further contributions from the gas-side kinetic and potential energy. However, since $\rho_G \ll \rho_G$, this contribution is negligible, and hence, the droplet energy E_D is a good approximation of the total system energy. Thus, "total energy" and "droplet energy" can be used interchangeably in what follows. The energy "budget" showing the different contributions to the droplet energy is shown in Fig. 8. Overall, the main contribution to the droplet energy after impact is the surface energy. Furthermore, surface energy is maximum when kinetic energy is minimum, and this coincides with maximum droplet spread.

The dependency of the surface energy and potential energy on the instantaneous droplet radius $r(t)$ is shown in Fig. 9. The surface energy can be very well approximated by treating the droplet as a 2D rectangular shape—the analogue for 3D axisymmetric droplets would be a disk, and this is a common approach in the literature.[4] In this context, the droplet extent is r and the droplet height is $h = A_0/(2r)$, where $A_0 = \pi R_0^2$ is the initial droplet area (volume). In this way, the approximate surface energy is $(1/\mathrm{Bo})(2r + 2h)$, and Fig. 9(a) shows excellent agreement between this rather crude approximation and the results of the numerical simulations. Furthermore, the gravitational potential energy is well captured by

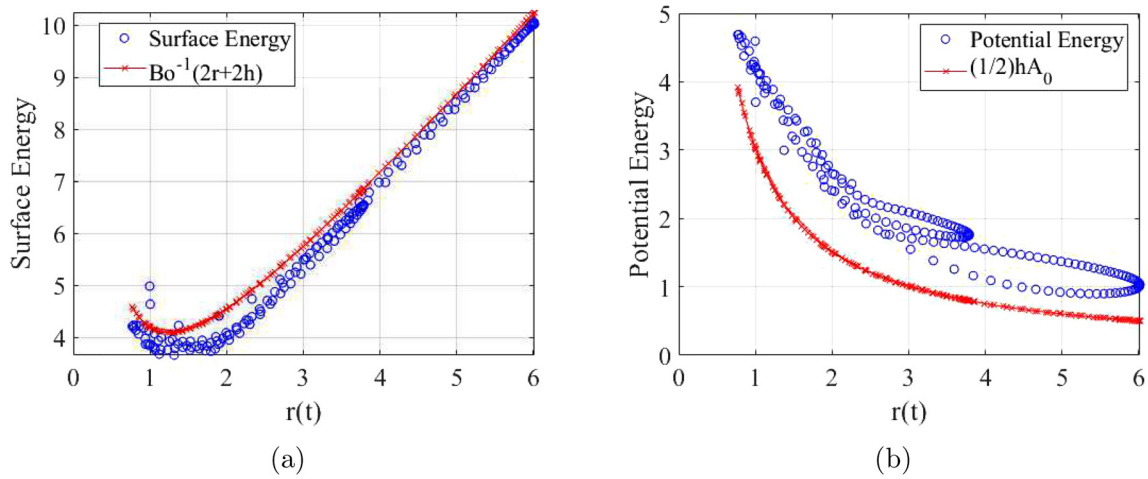

FIG. 9. Dependency of the different energy terms on the instantaneous droplet extent $r(t)$. (a) Surface energy and (b) potential energy. Parameters: $\vartheta_0 = 90^\circ$, Bo = 1.226, and Re = 578.0.

the same rectangular-shape approximation, with the gravitational potential energy estimated as $(h/2)A_0$ [Fig. 9(b)]—the factor of half is needed as this corresponds to the elevation of the droplet's center of mass. We use these findings in what follows to validate our correlations for β_{max}.

C. Correlations for the spreading radius

We carry over the correlations developed in Sec. II to the present case. As we are dealing with a smooth surface with no contact-angle hysteresis, we use the equilibrium contact angle in place of the advancing one. Also, as we are dealing with Bond-number scaling, some translation of the previous results is required. In particular, gravitational potential energy is now required in the energy balance. The elevation of the droplet center of mass is approximated by $h/2 = A_0/(4r_{max})$. In this way, the energy budget (4) becomes

$$\rho g H_0(\pi R_0^2) + 2\pi R_0\sigma = \sigma(\Pi - 2r_{max}\cos\vartheta_0) + \rho g(\pi R_0^2)d_c + \frac{a}{\sqrt{\mathrm{Re}}}\rho U_0^2\beta_{max}\sqrt{\beta_{max}-1}\,R_0^2 + b\rho g H_0(\pi R_0^2). \tag{30}$$

It is divided across by $\rho g R_0^3 \equiv \rho_L U_0^2 R_0^2$ to obtain

$$\pi(H_0/R_0) + \frac{2\pi}{\mathrm{Bo}} = \frac{1}{\mathrm{Bo}}\left[2\beta_{max}(1-\cos\vartheta_0) + \frac{\pi}{\beta_{max}}\right] + \pi\left(\frac{\pi}{4\beta_{max}}\right) + \frac{a}{\sqrt{\mathrm{Re}}}\beta_{max}\sqrt{\beta_{max}-1} + \pi(H_0/R_0)b. \tag{31}$$

We apply the correlation in Eq. (31) to Fig. 10. The parameters a and b are fitted only once to the case $\vartheta_0 = 90°$, to minimize the difference between β_{max} from the simulations and β_{max} from the correlation. Thereafter, the values of a and b are fixed, and the correlation (9) is used predictively, to determine the dependency of β_{max} on ϑ_0 at fixed Bo and Re. The results of the prediction are shown in Fig. 10. The values of a and b are given in Table III (the "two-parameter model" therein).

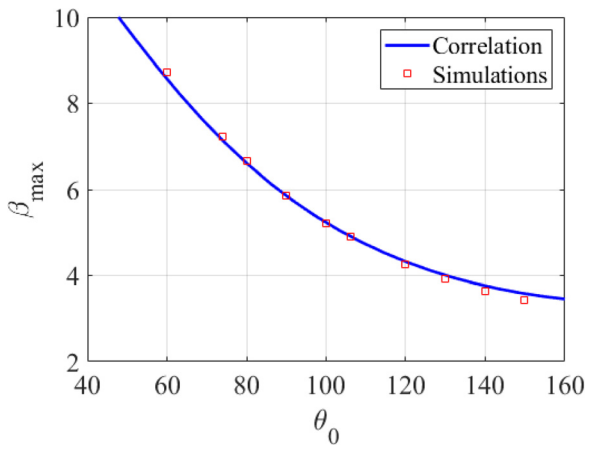

FIG. 10. Dependence of β_{max} on the static contact angle for fixed Bo = 1.226 and Re = 578.0. Squares: Simulations. Solid line: the correlation (31).

TABLE III. Estimated values of the fitting parameters for the models used.

	a	b	c
Two-parameter model	3.2096	0.3056	···
Three-parameter model	2.4963	0.5115	0.2738

To validate the correlation (31) further, we have repeated the simulation described previously (Sec. IV B) with $\vartheta_0 = 90°$, but with various values of the surface tension σ and liquid viscosity μ_L. In this way, we can investigate the effect of the Bond number and the Reynolds number of the maximum droplet spread. The results are shown in Fig. 11. Overall, there is good agreement between the correlation (9) and the simulation data over three orders of magnitude of Bo [panel (a)]. There is excellent agreement between the correlation and the simulation data over several orders of magnitude of Re [panel (b)]. This last result lends weight to the theory that the boundary layer is a main source of dissipation in the problem, with the boundary-layer dissipation term scaling as $\mathrm{Re}^{-1/2}$.

To improve the agreement between the simulation data and the theory in the case where Bo is varied, we have investigated further the flow pattern and dissipation pattern inside the droplet in the case of very high Bo (Fig. 12). These results may be compared with Fig. 5 (streamfunction) and Fig. 6 (dissipation). For the purpose of comparison, the same scales on the color bar are used throughout. The recirculation zone at high Bo is more organized in Fig. 12(a), compared to Fig. 5. Also, the gradient in the streamfunction is smaller in magnitude than before, and this can be seen by the sharp color gradient in the recirculation zone in Fig. 5, as opposed to the complete absence of such a color gradient in the recirculation zone in Fig. 12(a). All of these makes for a reduced level of dissipation, and this can be seen by comparing Fig. 6 with Fig. 12(b). Although boundary-layer dissipation is still an evidence in Fig. 12(b), overall, the amount of dissipation is less than before. This suggests that a reduction in the "head loss" dissipation term is appropriate at large values of Bo.

These differences call for a more detailed approach to the modeling of the droplet rim, which provides scope for future work. In the meantime, we model the change in the flow regime using a fitted model, $\Delta E_h = [b/(1+c\mathrm{Bo})]\rho g H_0(\pi R_0^2\lambda)$, where b and c are coefficients. As before, the model coefficients are obtained via non-linear least squares fitting (now a, b, and c). The non-linear optimization is done using constraints, such that $b \le 1$ and $c \ge 0$. These constraints are required for conservation of energy. The results of this updated model are shown in the inset of panel (a) in Fig. 11. Estimated parameter values are given in Table III (the "three-parameter model" therein).

V. COMPARISON WITH SIMULATIONS AND EXPERIMENTS: HEAD-ON COLLISION OF TWO DROPLETS

In this section, we consider the maximum spreading radius in the case of a head-on collision of two droplets. We examine the maximum spreading radius as obtained in simulations that already exist in the literature and supplement these with our own. We investigate the extent to which the simple correlation (15) for head-on collisions fits the numerical data. We also investigate whether the same simple correlation applies to experiments on the collision of quasi-2D cylindrical structures.

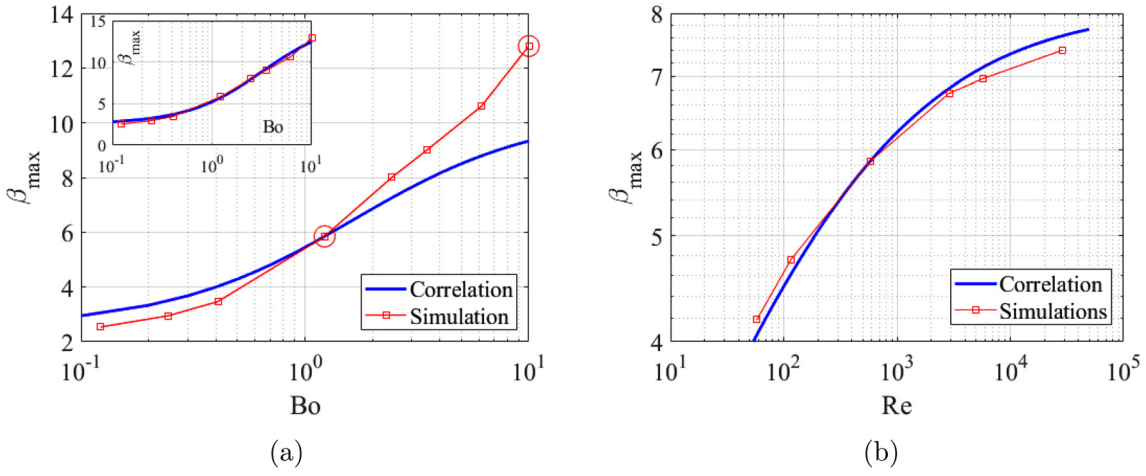

FIG. 11. Dependence of β_{max} on the parameters Bo and Re. Panel (a): fixed Re = 578.0 and varying Bo; panel (b): fixed Bo = 1.226 and varying Re. Squares: simulations. Solid line: the correlation (31) ("two-parameter model"). The inset in panel (a) shows the three-parameter model. The two parameter cases highlighted with the large open circles in the main plot in panel (a) have been singled out and the corresponding droplet profiles analyzed in more detail in the main text, specifically in Figs. 5, 6 and 12.

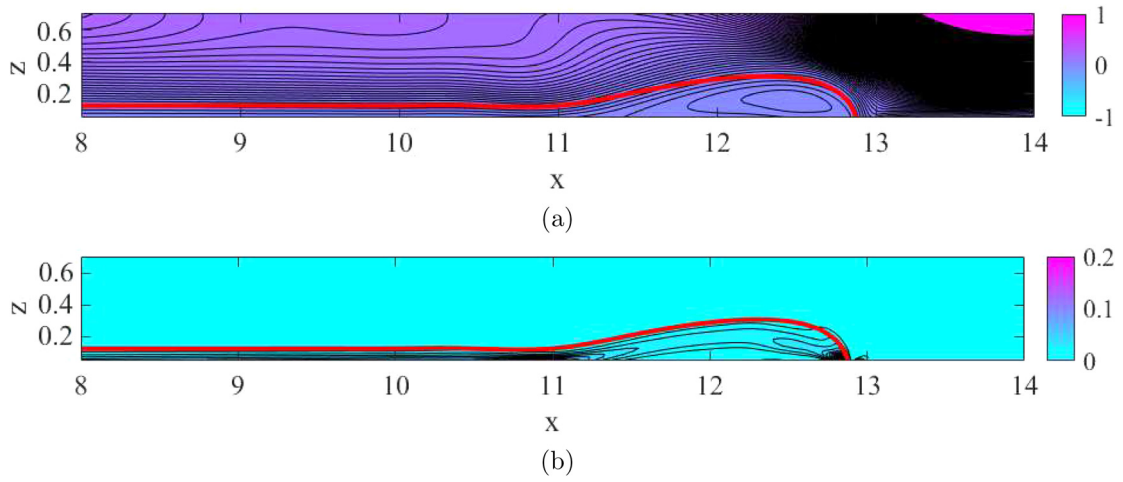

FIG. 12. Results at Bo = 10 and Re = 578, and $\vartheta_0 = 90^\circ$. (a) Instantaneous streamfunction at $t = 10.3$, near the point of maximum droplet spreading. (b) Instantaneous dissipation at the same time. To present both axes on the same scale clearly, only the range $8 \leq x \leq 14$ is shown. The symmetry point is at $x = 0$.

A. Comparison with simulations

We start by generating data using numerical simulations of a head-on collision between two 2D droplets, with a view to building up a database of simulation results to validate the correlation (15). We further compare our results with earlier results on head-on collisions by Wu *et al.*[19] For these purposes, we again use the diffuse-interface method and the numerical parameters in Sec. IV, with the initial condition shown in Fig. 13. Gravity is set to zero. The key dimensionless variables are, thus, $\mathrm{We} = \rho U_0^2 R_0/\sigma$ and $\mathrm{Re} = \rho U_0 R_0/\mu_L$.

Sample results are shown in Fig. 14. The results show droplet impact, spreading, and retraction, similar to what was observed in Sec. IV in the case of droplet impact on a solid substrate. Snapshots of the streamfunction are shown in Fig. 15. These show a recirculation zone in the rim, which gives rise to head loss. The maximum spreading radius as a function of We and Re is plotted in Fig. 16. Here, we also include the maximum spreading radius computed from the simulations by Wu *et al.*[19] In this same figure, we also compare the results of the numerical simulations to the correlation (15). For this reason, we fit the data from the paper of Wu *et al.*[19] to the correlation, for which non-linear least squares fitting yields $b = 0.5355$. The data involve the collation of results at various Reynolds numbers, on the understanding that the Weber-number effect is dominant in determining β_{max}. We use only those cases from the reference that do not involve film rupture, as such rupture in 2D is a numerical artifact. The results show that the energy loss can be well captured across the range of Weber numbers considered by a simple "head loss" factor b, independent of Reynolds number. Crucially, the neglect of the head loss leads to an over-prediction of the maximum spreading radius. Our own numerical

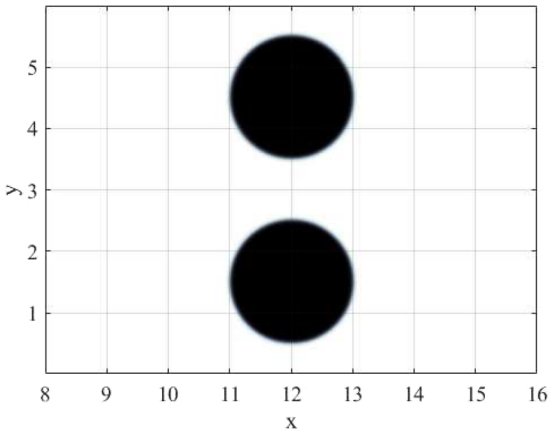

FIG. 13. Initial condition for the head-on collision. The upper droplet has a velocity $w = -U_0$, and the lower droplet has a velocity $w = +U_0$. The computational domain goes from $x = 0$ to 24; for better visibility, only a portion of this domain is shown.

results fall on the same curve, albeit that the slope of the trend line exhibits a mild Reynolds-number dependence at Re = 100. The same Reynolds-number dependence explains the off-trend datapoint of Wu *et al.* at We = 6.25, which corresponds to $\mathrm{Re} = \rho U_0 R_0/\mu = 10.75$.

B. Comparison with experiments

We also look at the performance of the model with respect to experimental data. Néel *et al.*[14] generate two toroidal liquid cylinders on the mm scale and engineer their head-on collision. Upon impact, a portion of the tori elongate to form cylindrical structures. The cylinders impact and spread in a direction perpendicular to the plane of the tori. The authors argue for the impact to be treated as the head-on collision of two cylindrical liquid structures. As such, the 2D droplet impact problem studied herein has an experimental analogue. Upon impact, the two liquid cylinders form a fused lamella, which elongates until a maximum length is attained. Beyond a critical Weber number, the lamella breaks up under a Rayleigh–Taylor instability in a process resembling droplet splash in the radially symmetric case.

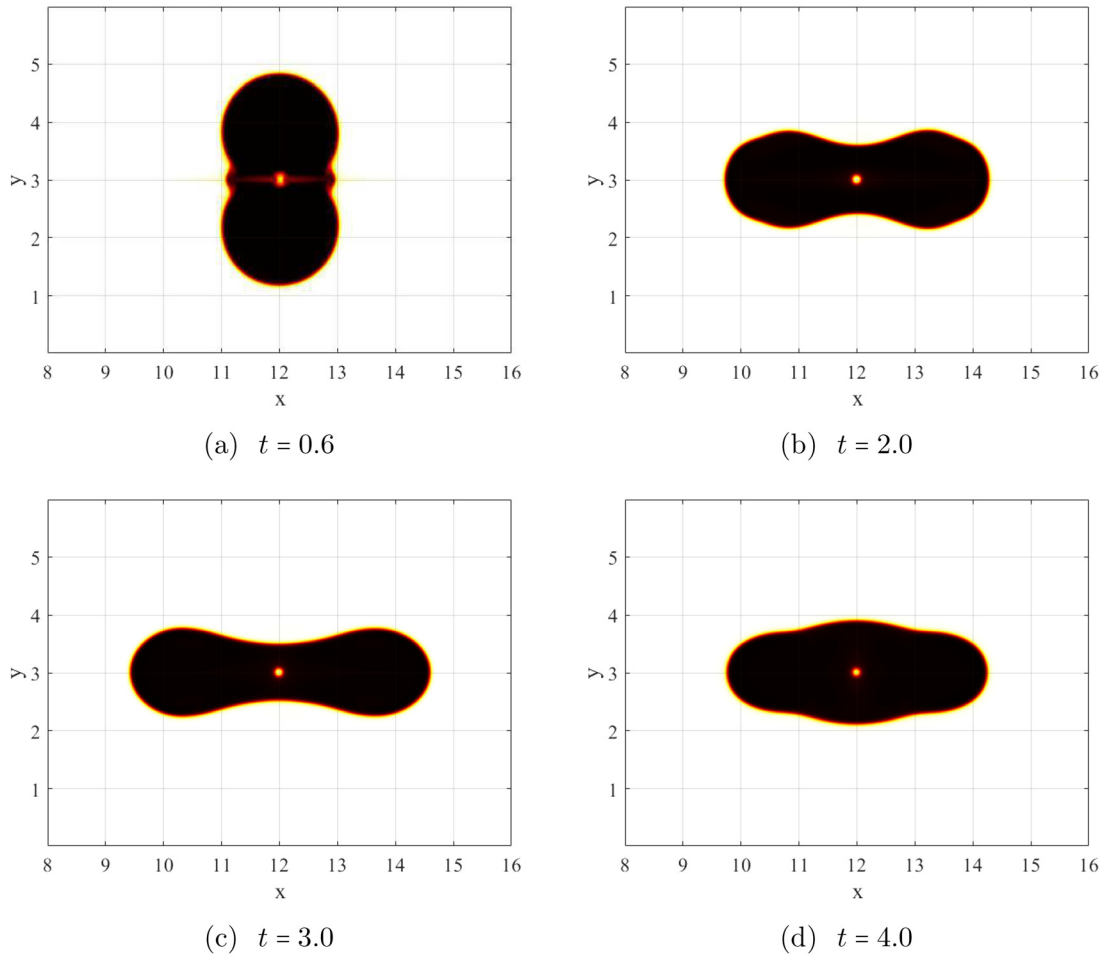

FIG. 14. Sequence of states for the head-on collision, for parameter values We = 1.225 and Re = 578. (a) $t = 0.6$, (b) $t = 2.0$, (c) $t = 3.0$, and (d) $t = 4.0$. Maximum spreading occurs at $t \approx 3.2$. The computational domain goes from $x = 0$ to 24; for better visibility, only a portion of this domain is shown.

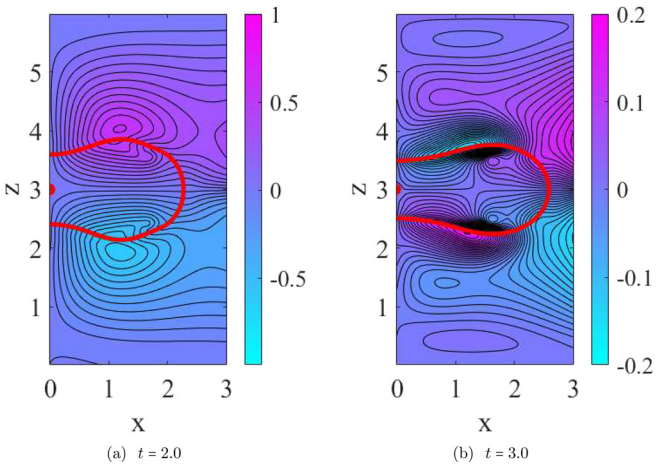

FIG. 15. Snapshots of the streamfunction in the case of head-on collision. (a) $t = 2.0$ and (b) $t = 3.0$. Parameter values: We = 1.225 and Re = 578.

We compare the experimental results by Néel *et al.*[14] with the model in Fig. 17, using $b = 0.5355$ as before. As such, we make no attempt to fit the correlation to the data and use only those model parameters determined from the previous simulation results. The correlation reproduces the trend in the data, but the quantitative agreement is poor. Expecting a simple 2D model to provide exact quantitative agreement in the case of a 3D toroidal impact problem may be unrealistic. The agreement may be improved by explicitly accounting for spontaneous surface dissipation in the energy budget (thus lowering the y-intercept of the curve in Fig. 17) and then refitting the model to the data. We do not pursue this approach here. Crucially, however, our correlation does exhibit the observed scaling behavior $R_{\max} \sim \mathrm{We}$ at a large Weber number. Such scaling is a signature of onset of 2D behavior in the spreading problem (3D spreading involves $R_{\max} \sim \mathrm{We}^{1/2}$ at large Weber number).

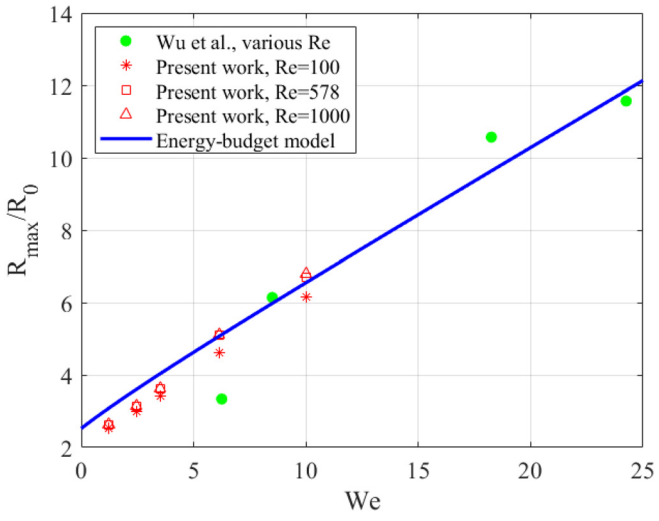

FIG. 16. Comparison between the energy-budget model (15) and the simulations by Wu *et al.*[19]

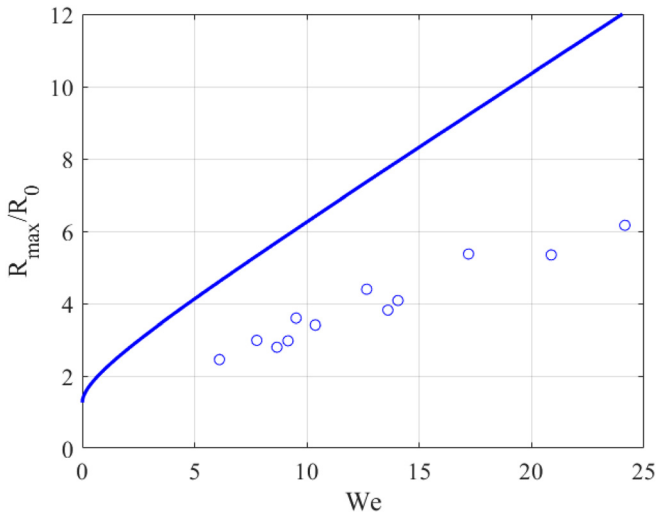

FIG. 17. Comparison between the model (15) (solid line) and the experiments by Néel *et al.*[14] (open circles), in the case of impact of two tori. The Weber number on the x axis is $\mathrm{We} = \rho U_0^2 R_0/\sigma$; the Weber number used in the reference is $8\rho U_0^2 R_0/\sigma$. The Reynolds number $\rho U_0 R_0/\mu_L$ is $O(10^5) - O(10^6)$.

Finally, we explore the overlap between the present energy-budget analysis and the simple 1D mechanistic model for the lamella extension $\beta_{\max}$ put forward by Néel *et al.*[14] The simple model in the reference predicts $\beta_{max} = 1 + (\pi/4)\mathrm{We}$. The slope here is the same as in Eq. (15), with $b = 0$. This is a drastic over-prediction of $\beta_{\max}$; hence, the head-loss factor is necessary to provide agreement between the experiments and the models.

VI. CONCLUSIONS

In summary, we have looked at the phenomenon of droplet spreading upon impact in 2D, in the case of impact on a solid substrate, as well as the head-on collision of two droplets. The setup we consider is a rather unusual physical scenario. However, it is studied in the computational literature as a testbed for similar but more computationally expensive simulations in three dimensions. Furthermore, recent experiments on liquid sheets suggest that such a setup may serve as a useful analogy for real 3D phenomena. Our main result is an energy-budget analysis, which gives a correlation for the maximum spreading radius as a function of We and Re. We have compared our correlation with the available results from the experimental and computational literature, supplemented by our own computational results where necessary.

In the case of droplet impact on a solid substrate, the computational data suggest at least two key dissipation channels. Boundary-layer dissipation in the lamella is important: without it, the model would greatly over-estimate the maximum extent of droplet spreading. A second source of dissipation is the so-called head loss. Appropriate modeling of these two loss channels leads to excellent agreement between the correlation and the numerical simulations, over several orders of magnitude of We and Re.

In the case of head-on collision of two droplets, energy dissipation is again required to make the energy-budget analysis agree with the experimental and numerical results. Although the simulations

show that no boundary layer is present, they do show a significant region of dissipation near the droplet "triple point" just after impact. A simple "head loss" argument can again be applied to the energy-budget analysis, whereby the dissipated energy is equated with a fraction of the initial kinetic energy. This approach gives excellent agreement between the theoretical prediction for the spreading radius and the numerical simulations, at sufficiently large Reynolds number.

The correlations introduced here agree well with the simulation data, over several orders of magnitude of We and Re. However, the argument based on head loss, while based on an earlier work on energy-budget analysis for droplet spreading,[22] still involves parameter fitting. A more physics-informed approach (such as a rim-lamella model, tailored to two dimensions) may be of use to estimate these parameters. As such, the present work—including the comprehensive database of numerical simulation results—may serve as a basis for future work for a more physics-informed approach to the head-loss calculation, involving a more detailed description of the rim-lamella dynamics.

ACKNOWLEDGMENTS

The authors acknowledge the Irish Centre for High-End Computing (ICHEC) for the provision of computational facilities and support (Project ID: ndphy119c). L.Ó.N. has also been supported by the ThermaSMART network. The ThermaSMART network has received funding from the European Union's Horizon 2020 research and innovation program under the Marie Sklodowska–Curie Grant Agreement No. 778104.

AUTHOR DECLARATIONS

Conflict of Interest

The authors have no conflicts to disclose.

Author Contributions

Lennon Ó Náraigh: Conceptualization (equal); Investigation (equal); Supervision (equal); Writing – original draft (equal); Writing – review & editing (equal). **Juan Mairal:** Conceptualization (equal); Methodology (equal); Writing – original draft (equal); Writing – review & editing (equal).

DATA AVAILABILITY

The data that support the findings of this study are available from the corresponding author upon reasonable request.

APPENDIX: ENERGY-BUDGET ANALYSIS

In this Appendix, we fill in the details of the derivations in Sec. II. We start with the expression for the pre-impact energy of the droplet. Quite simply, this is kinetic energy plus surface energy. The kinetic energy is $(1/2)MU_0^2$, where M is the mass of the droplet; hence, $M = \rho V$. Here, V is the volume of the cylindrical droplet, which quite straightforwardly is $\pi R_0^2 \lambda$; hence, the kinetic energy is $(1/2)(\pi R_0^2 U_0^2)\lambda$. Similarly, the surface energy is σA_{init}, where A_{init} is the surface area of the cylindrical droplet, which is $2\pi R_0 \lambda$; hence, the surface energy is $\sigma(2\pi R_0)\lambda$. Thus, the pre-impact energy is

$$E_{\text{init}} = \left[\frac{1}{2}\rho(\pi R_0^2)U_0^2 + 2\pi R_0 \sigma\right]\lambda, \tag{A1}$$

which is Eq. (2).

Similarly, the energy at maximum spreading is assumed to be due entirely to surface energy. The surface energy is

$$E_{\text{surf}} = \sum_i \sigma_i A_i, \tag{A2}$$

where the subscript runs over each of the three interfaces in the problem: $i = \{ls, as, al\}$, corresponding to the liquid–substrate, atmosphere–substrate, and atmosphere–liquid interfaces, respectively. In this case, the various surface tensions can be related through the Laplace–Young condition,

$$\sigma_{ls} + \sigma_{la}\cos\vartheta_Y = \sigma_{as}. \tag{A3}$$

Hence,

$$E_{\text{surf}} = \sigma_{la}(A_{la} - A_{ls}\cos\vartheta_Y) + (A_{ls} + A_{as})\sigma_{as}. \tag{A4}$$

Here, $A_{ls} + A_{as}$ is the total area of the substrate, which is a constant. Also, σ_{as} is a constant. Thus, the second term in the expression for the surface energy is a constant. As only energy differences are important, we choose instead to work with a modified expression for the surface energy, which omits this second constant term,

$$E_{\text{surf}} = \sigma(A_{la} - A_{ls}\cos\vartheta_Y), \quad \sigma \equiv \sigma_{la}. \tag{A5}$$

Finally, $A_{la} = \lambda\Pi$, where Π is the curved perimeter length of the base of the cylindrical droplet, and $A_{ls} = 2r_{\max}$. Thus,

$$E_{\text{surf}} = \sigma(\Pi - 2r_{\max}\cos\vartheta_Y)\lambda. \tag{A6}$$

In the main text, we look at simple scenarios where the moving (advancing) contact angle ϑ is the same as the equilibrium (Young) contact angle ϑ_Y, which gives

$$E_{\text{final}} = E_{\text{surf}} = \sigma(\Pi - 2r_{\max}\cos\vartheta)\lambda, \tag{A7}$$

which is precisely Eq. (3).

We also look at the energy dissipated in the viscous boundary layer. According to a standard expression,[21] this is given by

$$\Delta E_{\text{diss}} = \int\int_V \phi \, \mathrm{d}V\mathrm{d}t, \tag{A8}$$

where V is the droplet volume, and ϕ is the dissipation rate. The integration range over the time variable is between the onset of the boundary layer and maximum spreading, corresponding to a time interval τ. The dissipation rate inside the boundary layer is estimated as $\mu(U_0/\delta)^2$. Outside the boundary layer, $\phi = 0$. Hence, Eq. (A8) is estimated as follows:

$$\Delta E_{\text{diss}} \approx a\mu(U_0/\delta)^2(2r_{\max}\delta\lambda)\tau, \tag{A9}$$

where a is an $O(1)$ constant. Using $\tau \approx (r_{\max}/U_0) - (R_0/U_0)$ as in the main paper, this becomes

$$\Delta E_{bl} \approx \frac{2a}{\sqrt{\text{Re}}}\rho U_0^2 \beta_{\max}\sqrt{\beta_{\max} - 1}(R_0^2\lambda), \quad \beta_{\max} = \frac{r_{\max}}{R_0}, \tag{A10}$$

which is Eq. (5) in the main paper.

REFERENCES

[1]A. L. Yarin, "Drop impact dynamics: Splashing, spreading, receding, bouncing…," Annu. Rev. Fluid Mech. **38**, 159–192 (2006).
[2]P. J. Sáenz, K. Sefiane, J. Kim, O. K. Matar, and P. Valluri, "Evaporation of sessile drops: A three-dimensional approach," J. Fluid Mech. **772**, 705–739 (2015).
[3]S. Moghtadernejad, C. Lee, and M. Jadidi, "An introduction of droplet impact dynamics to engineering students," Fluids **5**(3), 107 (2020).
[4]S. Chandra and C. T. Avedisian, "On the collision of a droplet with a solid surface," Proc. R. Soc. London, Ser. A **432**(1884), 13–41 (1991).
[5]C. Antonini, A. Amirfazli, and M. Marengo, "Drop impact and wettability: From hydrophilic to superhydrophobic surfaces," Phys. Fluids **24**(10), 102104 (2012).
[6]G. Riboux and J. Gordillo, "Experiments of drops impacting a smooth solid surface: A model of the critical impact speed for drop splashing," Phys. Rev. Lett. **113**, 024507 (2014).
[7]I. V. Roisman, R. Rioboo, and C. Tropea, "Normal impact of a liquid drop on a dry surface: Model for spreading and receding," Proc. R. Soc. London, Ser. A **458**(2022), 1411–1430 (2002).
[8]J. M. Gordillo, G. Riboux, and E. S. Quintero, "A theory on the spreading of impacting droplets," J. Fluid Mech. **866**, 298–315 (2019).
[9]J. Fukai, M. Tanaka, and O. Miyatake, "Maximum spreading of liquid droplets colliding with flat surfaces," J. Chem. Eng. Jpn. **31**(3), 456–461 (1998).
[10]P. R. Gunjal, V. V. Ranade, and R. V. Chaudhari, "Dynamics of drop impact on solid surface: Experiments and VOF simulations," AIChE J. **51**(1), 59–78 (2005).
[11]J. Eggers, M. A. Fontelos, C. Josserand, and S. Zaleski, "Drop dynamics after impact on a solid wall: Theory and simulations," Phys. Fluids **22**(6), 062101 (2010).
[12]C. Josserand and S. T. Thoroddsen, "Drop impact on a solid surface," Annu. Rev. Fluid Mech. **48**, 365–391 (2016).
[13]S. Lejeune, T. Gilet, and L. Bourouiba, "Edge effect: Liquid sheet and droplets formed by drop impact close to an edge," Phys. Rev. Fluids **3**(8), 083601 (2018).
[14]B. Néel, H. Lhuissier, and E. Villermaux, "fines' from the collision of liquid rims," J. Fluid Mech. **893**, A16 (2020).
[15]H. Ding, P. D. Spelt, and C. Shu, "Diffuse interface model for incompressible two-phase flows with large density ratios," J. Comput. Phys. **226**(2), 2078–2095 (2007).
[16]S. Shin and D. Juric, "Simulation of droplet impact on a solid surface using the level contour reconstruction method," J. Mech. Sci. Technol. **23**, 2434–2443 (2009).
[17]A. Gupta and R. Kumar, "Two-dimensional lattice Boltzmann model for droplet impingement and breakup in low density ratio liquids," Commun. Comput. Phys. **10**(3), 767–784 (2011).
[18]Z. Wu and Y. Cao, "Dynamics of initial drop splashing on a dry smooth surface," PLoS One **12**(5), e0177390 (2017).
[19]Y. Wu, N. Gui, X. Yang, J. Tu, and S. Jiang, "A decoupled and stabilized lattice Boltzmann method for multiphase flow with large density ratio at high Reynolds and Weber numbers," J. Comput. Phys. **426**, 109933 (2021).
[20]A. H. Rafi, M. R. Haque, and D. H. Ahmed, "Two-dimensional analogies to the deformation characteristics of a falling droplet and its collision," Arch. Mech. Eng. **69**, 21–43 (2022).
[21]M. Pasandideh-Fard, Y. M. Qiao, S. Chandra, and J. Mostaghimi, "Capillary effects during droplet impact on a solid surface," Phys. Fluids **8**(3), 650–659 (1996).
[22]S. Wildeman, C. W. Visser, C. Sun, and D. Lohse, "On the spreading of impacting drops," J. Fluid Mech. **805**, 636–655 (2016).
[23]I. V. Roisman, "Inertia dominated drop collisions. II. An analytical solution of the Navier–Stokes equations for a spreading viscous film," Phys. Fluids **21**(5), 052104 (2009).
[24]E. Villermaux and B. Bossa, "Drop fragmentation on impact," J. Fluid Mech. **668**, 412–435 (2011).
[25]H. Park, W. W. Carr, J. Zhu, and J. F. Morris, "Single drop impaction on a solid surface," AIChE J. **49**(10), 2461–2471 (2003).
[26]H.-M. Huang and X.-P. Chen, "Energetic analysis of drop's maximum spreading on solid surface with low impact speed," Phys. Fluids **30**(2), 022106 (2018).
[27]K. Willis and M. Orme, "Binary droplet collisions in a vacuum environment: An experimental investigation of the role of viscosity," Exp. Fluids **34**(1), 28–41 (2003).
[28]M. Ewetola, R. Ledesma-Aguilar, and M. Pradas, "Control of droplet evaporation on smooth chemical patterns," Phys. Rev. Fluids **6**(3), 033904 (2021).
[29]L. Ó. Náraigh, P. Valluri, D. M. Scott, I. Bethune, and P. D. Spelt, "Linear instability, nonlinear instability, and ligament dynamics in three-dimensional laminar two-layer liquid/liquid flows," J. Fluid Mech. **750**, 464–506 (2014).
[30]L. Ó Náraigh, S. Shun, and A. Naso, "Flow-parametric regulation of shear-driven phase separation in two and three dimensions," Phys. Rev. E **91**(6), 062127 (2015).
[31]J. Fannon, J.-C. Loiseau, P. Valluri, I. Bethune, and L. Ó. Náraigh, "High-performance computational fluid dynamics: A custom-code approach," Eur. J. Phys. **37**(4), 045001 (2016).
[32]H. Ding and P. D. Spelt, "Wetting condition in diffuse interface simulations of contact line motion," Phys. Rev. E **75**(4), 046708 (2007).
[33]P. Yue and J. J. Feng, "Can diffuse-interface models quantitatively describe moving contact lines?" Eur. Phys. J. Spec. Top. **197**(1), 37–46 (2011).
[34]D. Legendre and M. Maglio, "Comparison between numerical models for the simulation of moving contact lines," Comput. Fluids **113**, 2–13 (2015).